Cellular deformation and intracellular stress propagation during optical stretching

Soo-Kng Teo,[1] Andrew B. Goryachev,[2] Kim H. Parker,[3] and K.-H. Chiam[1,*]
[1]*A*STAR Institute of High Performance Computing, Singapore, Singapore*
[2]*Centre for Integrative Systems Biology, School of Biological Sciences, University of Edinburgh, Edinburgh, United Kingdom*
[3]*Department of Bioengineering, Imperial College London, London, United Kingdom*
(Received 29 December 2009; published 26 May 2010)

Experiments have shown that mechanical stress can regulate many cellular processes. However, in most cases, the exact regulatory mechanisms are still not well understood. One approach in improving our understanding of such mechanically induced regulation is the quantitative study of cell deformation under an externally applied stress. In this paper, an axisymmetric finite-element model is developed and used to study the deformation of single, suspended fibroblasts in an optical stretcher in which a stretching force is applied onto the surface of the cell. A feature of our physical model is a viscoelastic material equation whose parameters vary spatially to mimic the experimentally observed spatial heterogeneity of cellular material properties. Our model suggests that cell size is a more important factor in determining the maximal strain of the optically stretched fibroblasts compared to the thickness of the actin cortical region. This result could explain the higher deformability observed experimentally for malignant fibroblasts in the optical stretcher. Our model also shows that maximal stress propagates into the nuclear region for malignant fibroblasts whereas for normal fibroblasts, it does not. We discuss how this may impact the transduction of cancer signaling pathways.

DOI: 10.1103/PhysRevE.81.051924 PACS number(s): 87.10.Kn, 87.17.Aa, 87.17.Rt

I. INTRODUCTION

Cells are subjected to mechanical stresses arising from their external environment throughout their lifetime. The understanding of the response of an individual cell to these stresses is important in many areas of biophysics. Indeed, mechanical stresses have been shown to regulate processes such as proliferation, migration, and differentiation [1–5]. While the exact mechanotransduction mechanisms involved are still not well understood, the quantitative study of how cells deform under mechanical stresses can yield important insights.

Malignant transformation of normal cells into the diseased state is known to induce morphological alterations in the cytoskeleton, leading to changes in a cell's viscoelastic properties [6,7]. Researchers using micropipette aspiration found a 50% reduction in the elasticity of malignantly transformed fibroblasts as compared to their normal counterparts [8]. Other researchers using atomic force microscopy [9] to investigate normal and cancerous endothelial cell lines have also reported that cancerous cells have a stiffness (as measured by the Young's modulus) about 1 order of magnitude lower than normal ones, which might be attributed to a difference in the organization of the cytoskeletons of the cells [10]. Results from other experimental techniques such as microplate manipulation [7] and optical tweezers [11] have also shown that cancerous cells are either less elastic or less viscous, depending on the measurement techniques and models used. Recent experiments have also shown that normal and malignantly transformed fibroblast cells deform (as measured by their optical deformability) to different extents when stretched optically [12–14]. The optical deformability is the strain normalized by the stretching force that the cell experienced (refer to [12] for detailed definition). This difference in the optical deformability has been exploited to construct diagnostic devices to screen for cancer cells [15–17].

In view of these experimental results, a numerical physical model that is able to describe the deformation of an individual cell, normal or cancerous, can give us important insights into the response of the cell when it is subjected to mechanical perturbations. The objective of this paper is to describe a viscoelastic, axisymmetric finite-element model of cell deformation and to discuss the results that we have obtained from applying this model to study the optical stretching of suspended fibroblast cells. While the use of viscoelastic models [18] to study cell deformation is not new, especially in the bioengineering literature [19–21], we consider a minimal physical model that yields features of the experimental results and are not concerned with precise and accurate models. In particular, we consider cellular heterogeneity in our model formulation. Previous viscoelastic models considered the cell as one homogeneous viscoelastic continuum which can be characterized by a single set of viscoelastic parameters (the number of parameters used varies from model to model). In our model formulation, we recognize that mammalian eukaryotic cells are heterogeneous and possess at least two distinct regions with different mechanical properties [22–25]: a cortical region (the network of actin filaments and associated cross-linking proteins that are tethered to the plasma membrane) that exhibits a predominately elastic response and a cytoplasmic region that is mainly free of such polymer scaffolds and exhibits a viscous response. Hence, we propose that the viscoelastic parameters in our model vary spatially to represent these two distinct cellular domains. Our approach is similar to that of the two-component model proposed by Laurent *et al.* [26]. In their model, the two components, namely. the submembranous "cortical" cytoskeleton and the "deep" cytoskeleton, were each represented by different sets of linear viscoelastic pa-

*chiamkh@ihpc.a-star.edu.sg

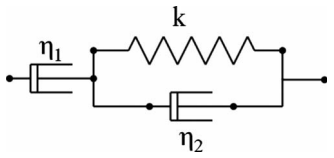

FIG. 1. Schematic of the viscoelastic three-parameter fluid model used to represent the material constitutive equation for the finite-element formulation. It consists of a linear dashpot connected in series with a Voigt element, which is a linear spring connected in parallel with a linear dashpot. Every discretized region within the cell is represented by such a three-parameter fluid model whose parameters $\{\eta_1, \eta_2, k\}$ can vary spatially.

rameters. However, in our approach, we allow for the spatial variation of the viscoelastic parameters within the two cellular domains, a feature that is not present in their model [26].

The optical stretching experiments were carried out with constant stress being applied to the suspended fibroblasts for different time intervals of 0.2, 2.5, and 10 s [14]. We have chosen to model the experiment for the intermediate time scale of 2.5 s because we believe that they are most likely to reveal the viscoelastic behavior of the fibroblasts. The cellular response at the short loading time scale of 0.2 s is likely to be dominated by the elastic characteristic of the fibroblasts since there is insufficient time for viscous dissipation to occur. Thus, the use of a viscoelastic model at this time scale may not be suitable. Similarly, the cellular response at the long loading time scale of 10 s is likely to be dominated by (a) dynamic remodeling of the cytoskeleton within the fibroblast as it stretches and (b) nonlinear stiffening response of the cytoskeleton elements such as the actin network [27,28] at large strains.

In this paper, we investigate the relative importance of cell size and thickness of the actin cortical region in determining the cellular deformability in the optical stretcher. The size differences between the malignantly transformed and normal fibroblasts affect the stress profile being applied on the fibroblasts. The differences in thickness of the cortical region, as can be seen from fluorescence imaging [12,15], directly affect the overall compliance of the fibroblasts. Therefore, these two factors are important in understanding why the deformation of malignantly transformed fibroblasts is different compared to normal fibroblasts. From our model, we show that the cell size contributes more significantly to this difference in deformability when compared to the thickness of the cortical region.

II. METHODS

A. Finite-element formulation

We use an axisymmetric formulation which allows us to capture the three-dimensional response of the cell in the optical stretcher with a two-dimensional model. Our analysis is done in the linear viscoelastic regime assuming that the cellular deformation is small compared to the overall size of the cell, so that nonlinear cellular stiffening is ignored. The governing equation of motion for the dynamic deformation of such a body is [29]

$$M\ddot{u} + \int_V B^T \sigma dV = f^{ext}, \tag{1}$$

where M is the mass matrix, B the strain-displacement matrix, σ the stress vector, f^{ext} the external load vector, and u the nodal displacement vector. To solve Eq. (1) for u, we need to define a constitutive equation relating σ to u. For this, we will assume that every discretized region within the body is a viscoelastic three-parameter fluid consisting of a linear dashpot connected in series to a Voigt element (refer to Fig. 1 and the Appendix for details of the formulation).

The choice of a viscoelastic fluid model is motivated by experimental observations that suspended fibroblasts deformed in the optical stretcher exhibit residual strains (i.e., do not return to their initial sizes on the time scale of obser-

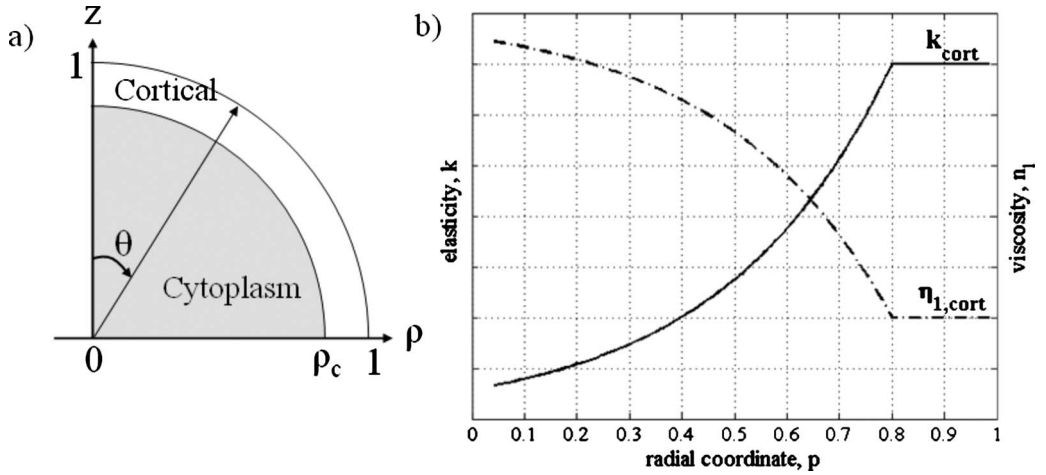

FIG. 2. Model geometry and spatial variation of material properties. (a) Schematic of the axisymmetric geometry of a cell of radius unity and definition of the radial coordinate ρ used in the finite-element simulation. Making use of symmetry, we need to only model one-quarter of the cell in our formulation. (b) Spatial variation of the material properties of the three-parameter fluid model with ρ. The elasticity k of the cell decreases exponentially away from the cortical region while the viscosities exhibit the opposite trend: η_2 varies in a similar manner as η_1 with respect to ρ. The cortical region is defined as the region $0.8 \leq \rho \leq 1$.

vation) after the removal of the stretching force [14]. For the loading time scale that we are interested in (2.5 s), the residual strain after stress relaxation (unloading) is about 20% of the peak strain during the loading phase (refer to Fig. 1(c) in Wottawah *et al.* [14]). This observation contradicts the use of a viscoelastic solid model to describe the deformation of the fibroblast as such a model does not exhibit any residual strain upon unloading. Instead, we chose a viscoelastic fluid model because its unloading response is qualitative similar to that shown in the optical stretcher experiment [14]. This is also another distinct difference between our model and other viscoelastic solid models used to describe micropipette aspirations in former studies [19,20].

B. Model parameters

The initial geometry of the cell in our model is represented by a sphere of radius unity in nondimensional units. We assume that the material properties of the cell are azimuthally isotropic. Then, we can introduce the radial polar coordinate ρ of a material point from the origin of the cell [Fig. 2(a)] so that the material property of each discretized region is a function of ρ [Fig. 2(b)].

For normal cells, we represent the actin cortical region as the region $0.8 \leq \rho \leq 1$, i.e., with a cortical thickness of 20%, and the cytoplasm as the region $0 \leq \rho < 0.8$ [15]. The thickness of the actin cortical region in our model is chosen to represent the average cortical thickness of normal fibroblasts (17%–23%) based on the analysis of fluorescence images straining for actin [15]. From these fluorescence confocal images (refer to Fig. 4 in Guck *et al.* [12]), we can see that the fibroblasts "…retains an extensive polymeric network even when in suspension…" [12] and that the actin filaments are highly localized to the cortical layer underneath the membrane. The intensity of the fluorescence in these images provides the spatial distribution of filamentous actin within the suspended fibroblasts and we can see that actin concentration decreases toward the center of the fibroblasts (away from the cortical region). Based on these images, we assumed that the actin filaments concentration in the cortical region to be constant and decreases linearly toward the center of the cell ($\rho \to 0$).

The elasticity of an isotropic, cross-linked network comprising semiflexible biopolymers such as actin have been studied extensively by MacKintosh *et al.* [30] and Gardel *et al.* [27]. For a given density of cross linkers, the network elasticity scales as a power law of the actin concentration with a coefficient of approximately 2.5 for both weakly cross-linked and tightly bundled (fully cross-linked) networks (refer to Figs. 1(a) and 2(c) in Gardel *et al.* [27]). However, Ananthakrishnan *et al.* [15] argued that such a model does not take into account the transient cross-linking dynamics (binding and unbinding) of the cross linkers and tend to overestimate the network elasticity. Instead, they proposed to take into account the chemical kinetics of the binding-unbinding of the cross linkers and derived a relationship for the network elasticity and actin concentration (refer to Fig. 3(b) in Ananthakrishnan *et al.* [15]). Following their approach, we proposed a simplified exponential function to describe the dependence of the network elasticity to actin concentration (to mimic the results presented in Fig. 3(b) in [15]) in our model. For the network viscosity, we assumed that its dependence on actin concentration follows the opposite trend as compared to the network elasticity. This is to approximate the predominately fluidlike flow response of the cytoplasm away from the cortical region. Combining our simplified function with the spatial variation of the actin concentration within the suspended fibroblast, we obtained the following equations for the spatial variation of the cellular elasticity k:

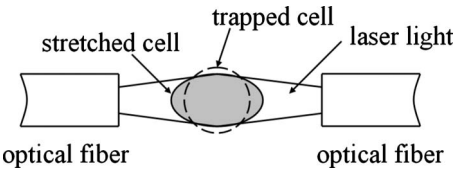

FIG. 3. Schematic of the optical stretching of a suspended cell. The stretching force is generated on the surface of the cell and acts normal to the cell surface. This stretching force can be approximated by Eq. (4) where n is a parameter that depends on the experimental setup and the size of the cell. Figure adapted from Ref. [16].

$$k = \begin{cases} k_{cyto} + (k_{cort} - k_{cyto}) e^{-\alpha(\rho_c - \rho)/\rho_c} & \text{for } \rho < \rho_c \\ k_{cort} & \text{for } \rho \geq \rho_c \end{cases} \tag{2}$$

and

$$\eta_i = \begin{cases} \eta_{i,cort} + (\eta_{i,cyto} - \eta_{i,cort})(1 - e^{-\alpha(\rho_c - \rho)/\rho_c}) & \text{for } \rho < \rho_c, \quad i = 1,2 \\ \eta_{i,cort} & \text{for } \rho \geq \rho_c, \quad i = 1,2, \end{cases} \tag{3}$$

where k_{cort} and $\eta_{i,cort}$ denote the elasticity and viscosity of the cell in the cortical region, k_{cyto} and $\eta_{i,cyto}$ denote the asymptotic basal elasticity and asymptotic plateau viscosity of the cell in the cytoplasm, α is a parameter that controls the rate of exponential increase or decrease, and ρ_c is the radial polar coordinate of the interface between the cortical region and cytoplasm. The variable ρ_c is set to 0.8 as described above. Thus we have a total of seven variable parameters (k_{cort}, k_{cyto}, $\eta_{1,cort}$, $\eta_{1,cyto}$, $\eta_{2,cort}$, $\eta_{2,cyto}$, and α) in our model. We note that our assumption for the choice of distribution of

TABLE I. Rheological properties of different cell types obtained experimentally. The cellular elasticity and viscosity reported spreads over a huge range, with about 2–3 orders of magnitude difference, depending on the cell type, the experimental techniques, and the model used to extract the rheological properties from the experimental data. The parameters (μ_0, μ_1, η_1) defined for the SLS below follows this convention: μ_0 is the elasticity of the spring element in parallel connection with the Maxwell element, μ_1 is the elasticity of the spring element in the Maxwell element, and η_1 is the viscosity of the dashpot in the Maxwell element.

Technique	Cell type	Elasticity (Pa)	Viscosity (Pa s)	Model
		Extracellular or whole cell measurements		
Magnetic twist [4]	Endothelial	2–10	n.a.	Secant
Optical tweezers [14]	Fibroblast	$G'=70-100$	$G''=25-50$ (Pa)	Three-parameter fluid (deduced)
Micropipette [20]	Endothelial	$\mu_0=\sim 45$, $\mu_1=\sim 75$	$\eta_1=\sim 3400$	SLS
Microplates [21]	Fibroblast	$\mu_0=\sim 960$, $\mu_1=\sim 510$	$\eta_1=\sim 13,000$	SLS
	Chondrocytes	$\mu_0=\sim 200$, $\mu_1=\sim 250$	$\eta_1=\sim 2500$	
Micropipette [19]	Nucleus	$\mu_0=550-700$, $\mu_1=500-750$	$\eta_1=5000-6000$	SLS
Micropipette [31]	Leukocyte	$\mu_0=\sim 0.75$, $\mu_1=\sim 24$	$\eta_1=\sim 33$	SLS
Cell poker [32]	Neutrophil	118	n.a.	Secant
Rheometer [33]	D. discoideum	$G'=55$	$G''=25$ (Pa)	Direct (10 rad/s)
AFM [34]	Platelet	1000–50000	n.a.	Hertz theory
Spont. retraction [35]	Fibroblast	1700	400000	Kelvin-Voigt
Magnetic tweezers [36]	Fibroblast	30000	2000	Four-parameter fluid
Micropipette [37]	Chondrocytes	$\mu_0=170-180$, $\mu_1=190-200$	$\eta_1=7500-8000$	SLS
		Intracellular measurements		
Magnetic tweezers [22]	Macrophage	20–735	210	Four-parameter fluid
LTM [25]	Epithelial	$G'=72$	$G''=38$ (Pa)	Direct (10 rad/s)
Magnetic twist [38]	Macrophage	~ 15	~ 2000	Secant

the cellular material properties holds only for cells in suspension and not for adhered cells.

The cell nucleus is omitted in our model formulation for simplicity given that the peak strain experienced by the cells in the optical stretcher (for the 2.5 s loading time scale that we are considering) is less than 6% [14]. We recognize that the cell nucleus possesses a very different set of mechanical properties from the other part of the cell and it plays a significant role in determining the overall response of the cell under any form of mechanical loading. However, under the small deformation regime that we are modeling, the contribution of the nucleus to the overall cellular response will likely be minimal and will not affect the qualitative trend of the results presented. The contribution of the nucleus to the overall cellular deformation will become increasingly important and significant at higher strain regime such as that observed for the 10 s loading time scale in the optical stretcher where the cellular strain reaches a quasistatic plateau. Wottawah *et al.* [14] attributed this observation to "…further fluidlike extension is prevented by an elastic component (evidence of significant contribution from the nucleus), which now dominates the temporal deformation."

The stresses generated by the optical stretcher on the surface of the cell ($\rho=1$) can be approximated by [16]

$$\sigma = \sigma_0 \cos^n \theta, \tag{4}$$

where σ is the stress normal to the cell surface, σ_0 is the peak stress along the laser axis (represented by the z axis) and is independent of the radius of the cell, θ is the azimuth angle measured relative to the laser axis [Fig. 2(a)], and n is a parameter that depends sensitively on the ratio of the half width of the laser beam at the cell to the initial radius of the cell (Fig. 3). Thus, a large value of n can indicate one of two experimental scenarios: either stretching the same cell by a laser that produces a more localized stress distribution or stretching a larger cell with the same laser. The value of the parameter n in Eq. (4) also depends on the refractive index of the cell relative to the medium. However, it has been shown that the refractive index for the malignant and normal fibroblasts used in the optical stretcher experiments are indistinguishable (refer to Fig. 3 in Ref. [12]). The forces in the optical stretcher are generated as a result of the differences in the dielectric constant of the cell and the medium and stably trap the cell in the middle of the optical stretcher. Thus, there is no need to consider effects such as cell-substrate adhesion or shape changes owing to the cell resting on the substrate.

C. Model validation

From Table I, we can see that the values of the cellular elasticity and viscosity reported in the literature by various researchers vary over a huge range. This disparity in the rheological properties obtained experimentally could represent biological diversity or could be due to the different experimental techniques used by the different researchers. The

underlying model used to extract the elasticity and viscosity from the experimental data could also contribute to the spread of the reported values.

Our strategy in choosing the parameters for our finite-element model is to constrain these parameters within certain physiological ranges using the reported values in Table I. For example, we note that most of the elasticity values reported using the standard linear solid (SLS) model in Table I falls with the range from 0.75 to 250 Pa [19,20,31,37] which is roughly consistent with the estimate of the elastic modulus ($G'=70-100$ Pa) obtained in Ref. [14]. Using these reported values, we constrained the parameters (k_{cort}, k_{cyto}) in our model within a range of 1–250 Pa. In a similar manner, we constrain the range of ($\eta_{1,cort}, \eta_{1,cyto}$) from 30 to 8000 Pa s.

The parameters ($\eta_{2,cort}, \eta_{2,cyto}$) are used to control the magnitude of the retardation time in the Voigt element of the three-parameter fluid model. This retardation time corresponds to the time-scale whereby the stress within the body is transferred and borne by the elastic component of the Voigt element and do not correspond to the physical viscosity of the cell. We assume that such transfer of stress occurs within a time-scale ranging from fractions of a second to seconds and therefore constrain the parameters ($\eta_{2,cort}, \eta_{2,cyto}$) so that the ratio of ($\eta_2/k$), the retardation time, falls within the range of 0.1–10 s.

Using the constrained range of the parameters ($k_{cort}, k_{cyto}, \eta_{1,cort}, \eta_{1,cyto}, \eta_{2,cort}, \eta_{2,cyto}$), we run our simulation for a total of 6 s with a loading time of 2.5 s to model the experimental setup in Wottawah *et al.* [14]. For each simulation, one pair of parameters is varied while the other pairs of parameters and α were kept fixed. The cellular strain (measured along the axis of the cell parallel to the direction of stretch) is obtained by dividing the change in the length along that axis by its original length. The strains obtained from our simulations are compared to the reported experimental data in a qualitative manner (we compare the trends of the strain development from our simulation to the actual experimental data). We did not carried out any quantitative analysis (such as least-squares minimization) on the simulation fit to the experimental data because of (1) the inherent uncertainty in the experimental data and (2) the rheological properties obtained from our model can only be considered bulk estimate of the cellular elasticity and viscosity. Hence, we believe that any quantitative error analysis would not be meaningful. The set of viscoelastic parameters that best fit the experimental trend are as shown in Table II.

We have also carried out a parameter sensitivity analysis for α [the parameter in Eqs. (2) and (3) that controls the rate of exponential increase or decrease of the cellular material properties from the cortical region to the cytoplasm region], while keeping the rest of the other parameters were kept fixed, to see how dependent our results are on this parameter. We observe that the strain response of the cell is dependent on the value of α chosen and the strain response curve obtained using a value of $\alpha=2.5$ gives us the best fit to the experimental data [refer to Fig. 4(a)] for the set of viscoelastic parameters shown in Table II. We also note that if we set α to zero, equivalent to modeling the cell as a homogeneous sphere, the fit to experimental data is significantly worse compared to that obtained using a nonzero value of $\alpha=1$ or 2.5. This suggests that spatial dependence of material properties is necessary to fit the experimental data. We also investigated if the exact functional form of this spatial dependence is important for determining the strain response of the cell in our simulation. Using $\alpha=2.5$ as our base case, we examine the effect of using a linear and a logarithmic variation in the spatial distribution of the cellular material properties [refer to Fig. 4(b)]. From Fig. 4(b), we can see that the strain response obtained in our simulation using the exponential variation gives the best fit to the experimental data as compared to the linear and logarithm variation. This supports our earlier assumption in choosing an exponential functional form to describe the spatial variation of the material properties.

TABLE II. Viscoelastic material parameters obtained by fitting our finite-element model to the experimental data.

	Value obtained by fitting to data for 2.5 s loading	
Parameter	Cortical	Cytoplasm
η_1 (Pa s)	1500	3000
η_2 (Pa s)	7.5	75
k (Pa)	150	30
Poisson's ratio	0.49	0.49

Our model differs from previous viscoelastic models [7,19,20] which considered the cell as a viscoelastic continuum represented by a standard linear solid characterized by a single set of viscoelastic parameters. In these previous models, there were no distinctions made between the cortical and cytoplasmic regions of the cell hence the viscoelastic parameters obtained from fitting to the experimental data are averages of the overall response of the cell. In our model, we distinguish between the cortical and cytoplasmic regions of the cell and are able to obtain two different sets of viscoelastic material parameters for these two distinct regions by fitting to the experimental data from the optical stretcher. This approach is similar to the core-shell model described in Ananthakrishnan *et al.* [15] which takes into account the different layers of the cell such as the nucleus, interior network, and the actin cortex. However, the core-shell model assumes that the different layers in the cell are represented by elastic layers which are different from our viscoelastic model. Furthermore, the equations used in solving the core-shell model are also restricted to idealized spherical geometry while our finite-element model has the capability to analyze less regular cellular geometry. The value of the cortical elasticity obtained from our model is comparable to the elasticity for the actin cortical shell from the core-shell model. This is not surprising since both models consider the cell to be comprised of distinct regions. However, comparison of the viscosity values between the two models is not possible since they assumed elastic properties.

The main advantages of our model as compared to previous models described above are twofold: (i) spatial distribution of the cellular material properties can be obtained by fitting to the experimental data and (ii) arbitrary cellular ge-

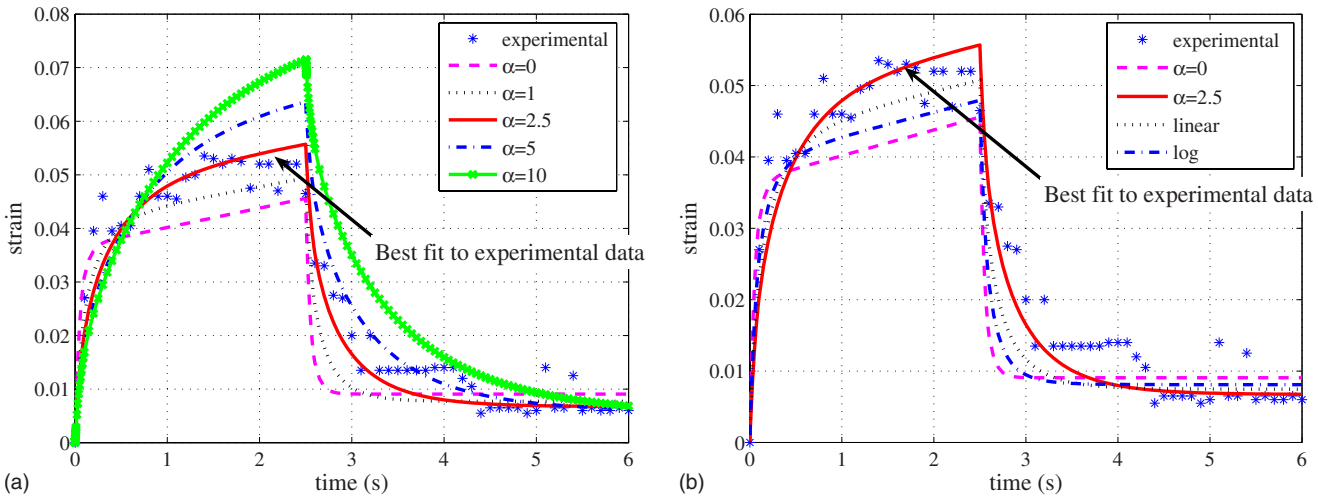

FIG. 4. (Color online) Sensitivity analysis to determine if our simulation results (the strain response along the long axis of the cell) are dependent on the values of the parameter α. (a) We observe that our results are dependent on the value of α chosen and the strain response curve obtained using a value of α=2.5 gives us the best fit to the experimental data. (b) The strain response obtained from using the exponential variation gives the best fit to the experimental data as compared to the linear and logarithm variations.

ometry can be analyzed for different experimental setups. First, the spatial distribution of the material properties obtained using our model can provide more information on cellular heterogeneity and its effects on stress propagation within the cell interior (more details will be described in Sec. III). Such analyses are not possible with previous viscoelastic models [7,19,20] as these models are one dimensional and hence do not include any spatial information. Second, the ability to analyzed arbitrary cellular geometry provides us the capability to model the actual cell shape in the experiment and not be restricted to idealized spherical or elliptical geometry. This capability is important in situations when the actual cell shape has a significant influence on the overall cellular deformation and the use of an idealized geometry can lead to inaccurate results.

In addition, the choice of the constitutive equation to describe the material properties in our model is also nonrestrictive. The choice of using a viscoelastic fluid model in our current analysis of the data from the optical stretching experiments [14] was motivated by experimental observation. For analysis of a different experimental setup, other elastic and/or viscoelastic solid-fluid models can be chosen to represent the material constitutive equation. It is also possible to assign different elastic or viscoelastic models to the different regions of the cell in the same analysis, such as the cortical region and the cytoplasm, should this need arises. This flexibility in choosing the appropriate constitutive equation in our model allows us to analyze data from not just the optical stretcher but also from other experiments.

The main disadvantage of our model is the larger number of variable parameters used in our fitting to the experimental data (we have a total of seven variable parameters) and the higher associated computational costs. In our analysis, we sought to reduce this computational cost by imposing an *a priori* constraint on the range of values for these parameters by doing a review of previous experimental studies (refer to Table I). In addition, the functional form for the spatial variation in the material properties is also open to question and we justified our choice of an exponential variation by referring to the analysis of Ananthakrishnan *et al.* [15]. However, the actual spatial heterogeneity within the cell can be more complex and affected by other factors such as the presence of microtubules, intermediate filaments, and other organelles. Nevertheless, we believe that these additional layers of heterogeneity are higher-order corrections to our simulation results and will not affect the overall qualitative trend presented here.

III. RESULTS

A. Maximal strain developed depends on size of suspended fibroblasts being stretched

From experiments [12,15], we know that the optical deformability of malignantly transformed fibroblasts is significantly higher than that of normal fibroblasts. From the data in these papers, we estimate that the mean optical deformability of malignantly transformed fibroblasts to be about 40% higher compared to normal fibroblasts. Guck *et al.* [12] suggested that the thickness of the actin cortical region plays an important role in determining this difference. We find that the thickness of the cortical region does indeed affect the cellular deformability but that cell size, through its effect on the stress profile is a more important factor in determining the deformation of the cell instead.

Table III lists some of the differences between malignantly transformed and normal fibroblasts. Normal fibroblasts generally have a larger radius (on average, 10% larger) and also a thicker actin cortical region as compared to malignantly transformed fibroblasts [15]. The larger radius of the normal fibroblasts means that the value of the parameter n in Eq. (4), which characterizes the spread of the stress distribution, is higher. Thus, under the same experimental setup, these normal fibroblasts are being subjected to a more localized stress distribution compared to the malignantly transformed fibroblasts [15]. The range of the parameter n

TABLE III. Material properties of suspended normal (NIH/3T3 and BALB/3T3) and malignantly transformed (SV-T2) fibroblasts in the optical stretcher experiment. The normal fibroblasts are subjected to a more localized stress distribution as characterized by a larger value of n as compared to the malignantly transformed fibroblasts. Approximately 95% of NIH/3T3 and 70% of BALB/3T3 fibroblasts are subjected to a more localized stress distribution with $14 \leq n \leq 24$ while 90% of SV-T2 fibroblasts are subjected to a broader stress distribution with $4 \leq n \leq 14$ [15].

Cell type	Normal	Malignantly transformed
Thickness of cortical region (%)	17–23	12–15
Parameter n in Eq. (4)	14–24	4–14

for normal fibroblasts is from 14 to 24. For malignantly transformed fibroblasts, it is from 4 to 14. We show quantitatively how these two factors, namely, the cell size (and equivalently, the spread of the stress distribution) and the relative thickness of the cortical region, affect the cellular deformation. For our analysis, we assume that the material properties of the malignantly transformed fibroblasts are identical to those of normal fibroblasts. This is to simplify our analysis and to determine the relative contribution of the cortical thickness and cell size to the cellular deformation. In reality, we would expect the malignant fibroblasts to possess lower elasticity and viscosity compared to the normal fibroblasts [7,8].

We start by considering the effect of the parameter n on the deformation of a solid homogeneous elastic sphere subjected to an axisymmetric stress on the surface given by Eq. (4). This would correspond to optically stretching homogeneous elastic beads of varying sizes with a fixed laser width in the experimental setup. The justification for this analysis is to test our hypothesis that the cell size (through its effect on the spread of the stress distribution) affects the cellular strain in the optical stretcher.

Following the approach in Ananthakrishnan *et al.* [15] [refer to Eqs. (1)–(3) and (A1) in that reference], we can compute the analytical strain at the surface of the sphere as a function of θ, the azimuth angle measured relative to the laser axis (z axis), and the elastic properties of the sphere for different values of n. Denoting the strain along the laser axis as ε_z and that perpendicular to the laser axis as ε_r, we compared our finite-element simulation results for a homogeneous elastic sphere with the analytical solution for $n=2$, 4, and 6. The results are summarized in Table IV. We can see that there is close agreement between our simulation results and the analytical solutions with errors of less than 1%. We further extend our simulation for values of n ranging from 2 to 24 and plot the results in Fig. 5. We see that the strain along the laser axis (ε_z) for an elastic sphere is sensitively dependent on the parameter n. For $14 \leq n \leq 24$, corresponding to a larger cell or a more localized stress profile, ε_z is smaller compared to the case of $4 \leq n \leq 14$, corresponding to a smaller cell or a broader stress profile. In Fig. 5, we see that ε_z for $n=4$ (which represents the stress profile experienced by the smallest, malignant fibroblasts) is approximately one-third larger compared to ε_z for $n=24$ (which represents the stress profile experienced by the largest, normal fibroblasts). This observation shows that the profile of the surface stress as represented by the parameter n in Eq. (4) plays an important role in the deformation of the cell. Our model prediction in this section can be tested experimentally by optically stretching homogeneous elastic spheres of varying sizes using the optical stretcher.

TABLE IV. Strain for a solid homogeneous elastic sphere along the laser axis ε_z and that perpendicular to the laser axis ε_r. The simulation results from our finite-element model are compared against the analytical solution for values of $n=2$, 4, and 6. There is close agreement between simulation and analytical solutions for this idealized case with errors of less than 1% in both ε_z and ε_r.

	Stretching profile: $\sigma=\sigma_0 \cos^n \theta$		
Parameters	$n=2$	$n=4$	$n=6$
Simulation results obtained from finite-element simulation			
ε_z	0.0246	0.0247	0.0233
ε_r	−0.0117	−0.0087	−0.0068
Analytical results for a solid homogeneous elastic sphere			
ε_z	0.0244	0.0245	0.0231
ε_r	−0.0117	−0.0087	−0.0068
Error in strain (%)			
ε_z	0.73	0.64	0.62
ε_r	−0.08	−0.08	−0.08

We next investigate the effects on the strain (ε_z) of varying the cortical thickness and the parameter n separately us-

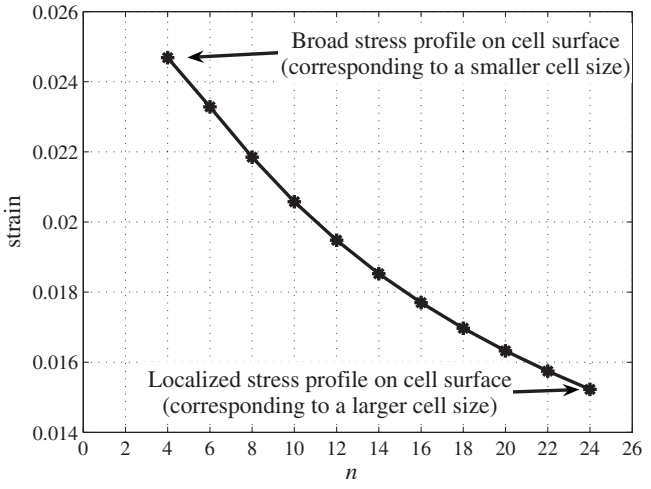

FIG. 5. Effects of surface stress profile on strain experienced for a solid homogeneous elastic sphere. The strain along the laser axis, denoted by ε_z (solid line), for a solid homogeneous elastic sphere subjected to a surface stress profile as given in Eq. (4) computed using our finite-element model. We can see that ε_z is sensitively dependent on the parameter n in Eq. (4). For larger values of n (corresponding to a more localized stress profile), ε_z is smaller compared to the case of a smaller value of n (corresponding to a broader stress profile).

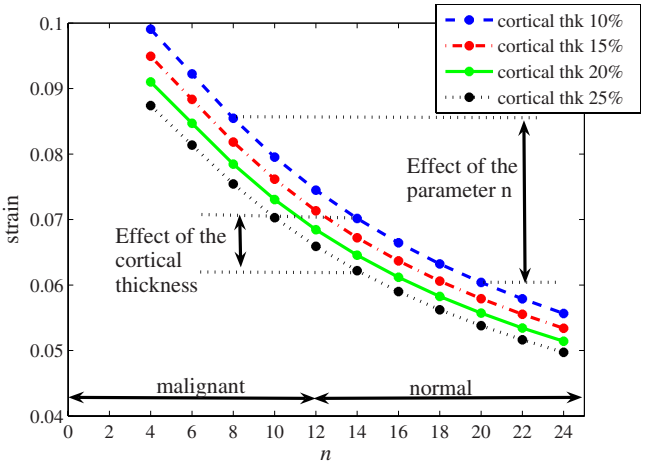

FIG. 6. (Color online) Effect of cortical thickness and surface stress profile on strain experienced for a suspended fibroblast. We investigated the effects of varying either the cortical thickness or the surface stress profile, represented by the parameter n in Eq. (4), on the strain (ε_z) obtained at 2.5 s using our viscoelastic finite-element model. First, cortical thickness was varied from 10% to 25% (dashed blue line: 10%, dotted-dashed red line: 15%, solid green line: 20% and dotted black line: 25%) while keeping all other parameters constant. Next, the parameter n was varied from 4 to 24. The strain (ε_z) is more sensitive to the variation in the parameter n than variation in the cortical thickness and is smaller for larger values of n compared to those cases with smaller values of n. This shows that cell size contributes more to cellular deformation as compared to cortical thickness.

ing our three-parameter fluid model. First, we varied the thickness of the cortical region from 10% to 25% while keeping the other parameters unchanged. Next, we varied the value of n from 4 to 24 while keeping the other parameters unchanged. The material properties of the cell used for this set of simulations are those shown in Table II which we obtain from fitting the 2.5 s loading experiment. From Fig. 6, we see that the strain ε_z is less sensitive to the variation in the cortical thickness as compared to the parameter n. In making our comparison, we note that the change in ε_z when we vary the cortical thickness is fairly independent of the values of the parameter n. Hence, we decided to choose one value of n (we used $n=14$ in Fig. 6 which is the midrange value for the parameter n) to illustrate the typical effect of varying the cortical thickness on ε_z. Similarly, we have chosen $n=8$ and $n=20$, which are the midrange values for characterizing the stress profile experienced by the malignant and normal fibroblasts, respectively, to illustrate the effect of the parameter n on ε_z. We also observe that the strains ε_z are smaller for a larger value of n when compared to those of a smaller n which is similar to the trend exhibited by the homogeneous elastic sphere. Thus, our simulation results are in agreement with the experimental evidence that the smaller malignant cells deform more compared to their normal counterparts. However, it is the cell size that contributes more to this cellular deformation than the cortical thickness.

B. Extent of intracellular stress propagation depends on size of suspended fibroblasts being stretched

In this section, we study the von Mises stress distribution within the cell as a function of the cell size [29]. In particular, we want to see how far the stress propagates into the cytoplasm when (a) malignant fibroblasts are subjected to a broad surface stress distribution and (b) normal fibroblasts are subjected to a localized surface stress distribution. The von Mises stress from our simulation is computed using the spring element in the three-parameter viscoelastic fluid model. The details of the simulation are: the material properties of both the normal and malignant fibroblasts are set to identical values (shown in Table II). The thickness of the actin cortical region is set to 20% for normal cells and 15% for malignant cells [15].

In Fig. 7, we show the von Mises stress distribution at 2.5 s for the two simulations. The two surface stress profiles are represented by (a) $n=24$ (localized stress distribution) denoting normal cells and (b) $n=4$ (broad stress distribution) denoting malignant cells. For (a), we see that the regions with the highest von Mises stress concentration occur at a region just beneath the cortical region. This observation is distinctly different from that observed for (b) in which the region of highest von Mises stress is in the perinuclear region of the cell.

IV. DISCUSSION

A. Influence of cell size on the maximal strain

The results of our simple physical model suggest that, to improve the discriminating capability of the optical stretcher as a diagnostic tool, cells should be sorted based on size prior to undergoing optical stretching. By doing so, cells of approximately the same size will be subjected to similar stress profiles and any differences in their optical deformability will more accurately reflect an inherent variation in their mechanical properties, hence enabling the device to better differentiate between the normal and cancerous phenotypes of the cells being tested.

In our simulations, we have assumed that both the malignant and normal fibroblasts possess identical material properties in our numerical calculation. If we had incorporated a lower elasticity and viscosity in our model for the malignant fibroblast, the difference in the cellular strain obtain between the normal and malignant fibroblasts would have been even larger. Thus, our model predictions do not contradict the experimental results of Guck *et al.* [12]. Rather, we have shown that the cellular size, through its effect on the spread of the stress distribution, contributes relatively more to the cellular deformation as compared to the cortical thickness.

Our results also rest upon the assumption that the optical properties are homogenous in both the malignant and normal cells. It is possible that there will be regions in the cell with different optical properties, which could lead to a different distribution of stress on the surface. One possible example is a smaller malignant fibroblast with a relatively large nucleus with higher refractive index, which could lead to a stronger focusing of the light passing through the cell and conse-

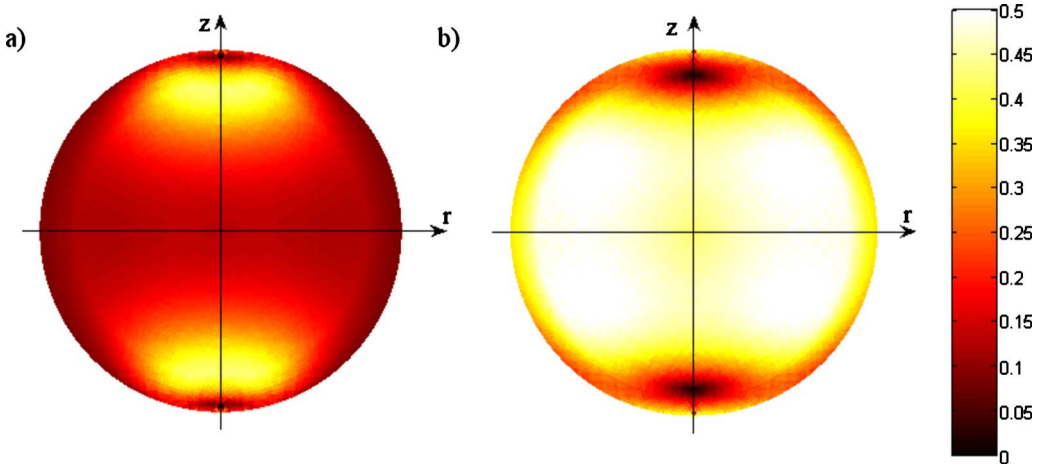

FIG. 7. (Color online) Plot of von Mises stress distribution for normal and malignant fibroblasts. Lighter colors denote higher stress magnitudes while darker colors denote lower stress magnitudes. The von Mises stress at 2.5 s is obtained from finite-element simulation for (a) normal fibroblasts subjected to a localized surface stretching ($n=24$) and (b) malignant fibroblasts subjected to a broad surface stretching ($n=4$). For the localized stress distribution, we see that the regions with the highest von Mises stress concentration occur at a region just beneath the cortical region. This observation is distinctly different from that observed for the broad stress distribution in which the region of highest von Mises stress is in the perinuclear region of the cell.

quently a more localized stress distribution than assumed. In this case, the explanation for the different deformability between the normal and malignant fibroblasts suggested from the parameters in our model might not hold. Given the complexity of the actual stress distribution on the cell surface during the experiments, we believe that our model can still contribute to the understanding of the differences in cellular response between malignant and normal fibroblasts in the optical stretcher despite our simple assumptions.

B. Influence of cell size on stress propagation

The size of the suspended fibroblasts, through its effect on the surface stress profile, affects the intracellular stress propagation and distribution. This observation is useful as it allows us to visualize the stress propagation from the cortical region through to the cytoplasm as a function of the surface stretching profile. We believe that the two distinct regions of high von Mises stress concentration for the localized stretching profile could be a result of the short length-scale force transmission characteristics of the cortical region. When a mechanical loading applied to the cell is concentrated on a localized region of its cortex or cytoplasm, the cellular response will depend on the region being probed. Experimental techniques that apply a localized loading include atomic force microscopy, magnetic bead twisting, and micropipette aspiration techniques. At the other extreme, when the entire cell is subjected to mechanical stress, such as a shear flow or microplate manipulation, the cellular response will depend upon the overall compliance of the entire cell. This could be an explanation for the huge spread of experimental values reported for the coefficients of elasticity and viscosity. The results of the different measurements will depend not only on the model used to extract the relevant elastic or viscous parameters but also, to a large extent, on the region of the cell being probed and the extent of the probing mechanisms (whether it acts over a localized region or the entire cell).

We also believe that different mechanosensitive signaling pathways may be activated in the optical stretching experiment as a result of the differences in the relative stress distribution within the interior of the suspended cell. One possible mechanism is for the cell to upregulate the concentrations of actin binding proteins in response to signaling pathway that are mediated through the stretch activated channels on the membrane surface [39,40]. The locations on the cell membrane where such channels are activated could depend on the relative stress distribution induced on the cell surface. We postulate that these activated channels then transduce the external mechanical forces into intracellular biochemical signals through the increase in the cytosolic Ca^{2+} level [41] which in turn triggers a cascade of signaling pathways [42]. One such possible signaling pathway is the Rho/Rho-kinase transduction pathway which is involved in the cytoplasmic stiffening of adherent fibroblasts subjected to shear flow [43]. We thus suggest that fluorescent tagging be done on actin binding proteins such as filamin A to investigate how their concentration in the cortical regions varies as the suspended fibroblasts are subjected to different stretching profiles. Such investigations could allow us direct comparison of our simulation results of the location of high von Mises stress to experimental observations on the regions of high activity of actin-binding proteins.

V. CONCLUSION

We have described a viscoelastic, axisymmetric finite-element model that takes into account the spatial heterogeneity of cells and have shown that our model can be used to simulate the stretching of suspended fibroblast cells in the optical stretcher. The first result is that the higher optical deformability observed for malignant fibroblasts [12] can be explained by the difference in the surface stress profile

(which is related to the cell size). We have shown that the parameter n which describes the profile of the surface stress is a more important factor in determining the radial deformation of the cell than the thickness of the actin cortical region. This implies that cells with a smaller radius will experience more stretching compared to cells with a larger radius in the optical stretcher due to the broader stress profile experienced by the smaller cells.

The second result suggests that the modes of stress propagation into the cytoplasm are different for normal and malignant fibroblasts. Our simulation shows that the von Mises stress distribution within the cell is dependent on the surface stress profiles used. For the localized stretching profile, the regions with the highest von Mises stress concentration occur at a region just beneath the cortical region. This pattern is distinctly different from that observed for the broad stress distribution in which the region of highest von Mises stress is in the perinuclear region of the cell. The implication of our observation is that different mechanosensitive pathways are activated in the optical stretching experiment as a result of the differences in the intracellular stress distribution. The activation of these different pathways can lead to different molecular level expression of proteins that in turn affect the mechanistic properties of the fibroblasts being stretched. Currently, there is no existing theory that can quantitatively link mechanistic perturbation to molecular level expression in the cytoplasm. We believe that our modeling, combined with other experimental techniques such as molecular imaging, has the potential to contribute further in understanding mechanotransduction.

ACKNOWLEDGMENTS

We thank J. Guck and F. Wottawah for insightful discussions about their experiments and acknowledge the financial support of the Agency for Science, Technology, and Research (A*STAR) of Singapore under the A*STAR-Imperial Partnership Ph.D. Program.

APPENDIX: FINITE-ELEMENT FORMULATION

The governing equation for a viscoelastic three-parameter fluid consisting of a linear dashpot connected in series to a Voigt element (refer to Fig. 1) in one dimension is given by [18]

$$\eta_1 \frac{\partial \varepsilon(t)}{\partial t} + \frac{\eta_1 \eta_2}{k} \frac{\partial^2 \varepsilon(t)}{\partial t^2} = \sigma(t) + \frac{(\eta_1 + \eta_2)}{k} \frac{\partial \sigma(t)}{\partial t}, \quad (5)$$

where ε is the time-dependent strain that is a dimensionless form of the nodal displacement u, σ is the time-dependent stress, η_1 is the viscosity of the linear dashpot in series connection with the Voigt element, and η_2 and k are the viscosity and elasticity of the linear dashpot and linear spring of the Voigt element.

In higher dimensions, the constitutive equation becomes more complicated to write down. Instead, we should use the approach outlined in Kaliske and Rothert [44] and consider two SLSs (refer to Fig. 8) connected in series in order to mimic the response of the three-parameter fluid in higher dimensions (refer to Fig. 9). We used a different set of notation here to represent the parameters of the two SLS in series to prevent confusion with the parameters for the three-parameter fluid model.

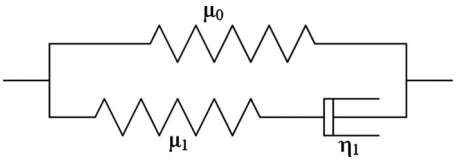

FIG. 8. Representation of a standard linear solid model. It consists of a single-spring element (μ_0) in parallel connection with a Maxwell model. The Maxwell model consists of another spring element (μ_1) in series connection to a dashpot element (η_1).

The representation of the three-parameter fluid model can be done through the appropriate selection of parameters in the SLS models to mimic both the fluidlike response of the dashpot and the creep response of the Voigt element for the time intervals that we are interested in. First, to mimic the fluidlike response of the dashpot, we need to set the value of the single spring element (μ_{01}) in the first SLS (refer to Fig. 9) to approaching zero and set the value of the spring element in the Maxwell model (μ_{11}) to approaching infinity. This has the effect of "short-circuiting" the contributions of these two spring elements in the first SLS for the time intervals that we are interested in. Next, to mimic the creep response of the Voigt element, we will need to set the value of the spring element in the Maxwell model (μ_{12}) in the second SLS (refer to Fig. 9) to approaching infinity. This also has the effects of short-circuiting the contribution of that spring element in the second SLS. Using Boltzmann's principle of superposition [18], we are able to sum the response of the two SLS to mimic the response of the three-parameter fluid model.

The development of the finite-element formulation for the SLS model (refer to Fig. 8) starts from the general integral representation of linear viscosity as a one-dimensional equation as shown below:

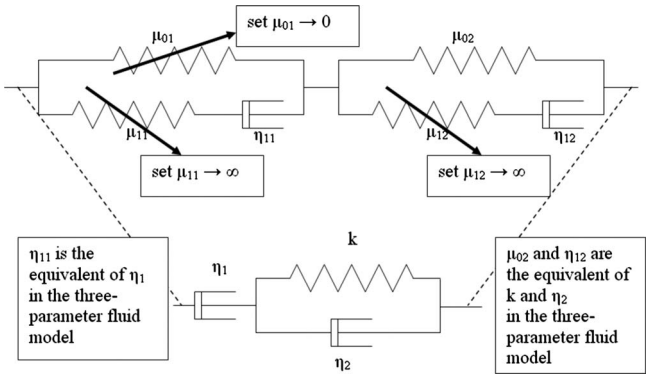

FIG. 9. Representation of the three-parameter fluid model using two standard linear solids arranged in series. The value of the single spring element (μ_{01}) in the first SLS is set to approaching zero while the values of the spring elements in the Maxwell model (μ_{11} and μ_{12}) for both SLS are set to approaching infinity. These have the effect of "short-circuiting" the contributions of these spring elements to the response of the two SLS in series, thereby allowing us to mimic the response of the three-parameter fluid model.

$$\sigma(t) = \int_0^t \Gamma(t-s)\frac{\partial \varepsilon(s)}{\partial s} ds, \tag{6}$$

$$\Gamma(t-s) = \mu_0 + \mu_1 e^{-(t-s)/\tau_1}, \tag{7}$$

$$\tau_1 = \frac{\eta_1}{\mu_1}, \tag{8}$$

where $\Gamma(t-s)$ is the relaxation function and τ_1 is the relaxation time for the Maxwell element in the SLS. Following the approach outlined in Kaliske and Rothert [44], splitting the integral into an elastic and a viscoelastic contribution leads to the elastic stress component $\sigma_0(t)$ and the internal stress equivalent variable $h_1(t)$ as shown below:

$$\begin{aligned}\sigma(t) &= \int_0^t \mu_0 \frac{\partial \varepsilon(s)}{\partial s} ds + \int_0^t \mu_1 e^{-(t-s)/\tau_1} \frac{\partial \varepsilon(s)}{\partial s} ds \\ &= \mu_0 \varepsilon(t) + \int_0^t \mu_1 e^{-(t-s)/\tau_1} \frac{\partial \varepsilon(s)}{\partial s} ds \\ &= \sigma_0(t) + h_1(t).\end{aligned} \tag{9}$$

The internal stress equivalent variable $h_1(t)$ can be evaluated using the recursive formula given by Ref. [44] and as shown below:

$$h_1^{n+1} = e^{-\Delta t/\tau_1} h_1^n + \gamma_1 \frac{1 - e^{-\Delta t/\tau_1}}{\frac{\Delta t}{\tau_1}} [\sigma_0^{n+1} - \sigma_0^n], \tag{10}$$

$$\gamma_1 = \frac{\mu_1}{\mu_0}. \tag{11}$$

This recursive determination of the current h_1^{n+1} requires the quantities σ_0^n and h_1^n of the preceding time step n and, therefore, they have to be stored in a database. The shown strain-driven integration algorithm is unconditionally stable for small and large time steps and it is second-order accurate.

The extension of Eq. (9) to a fully three-dimensional approach is easily performed by introducing tensor quantities. In a multiaxial stress state, the total stress tensor σ^{n+1} for a linear elastic Maxwell material is determined from the elastic contribution σ_0^{n+1} and from the internal stress variables h_1^{n+1}. Thus, we can write the stress tensor σ^{n+1} in a multiaxial stress state as follows:

$$\sigma^{n+1} = \sigma_0^{n+1} + h_1^{n+1}, \tag{12}$$

$$\sigma_0^{n+1} = D^e \varepsilon^{n+1}, \tag{13}$$

$$h_1^{n+1} = e^{-\Delta t/\tau_1} h_1^n + \gamma_1 \frac{1 - e^{-\Delta t/\tau_1}}{\frac{\Delta t}{\tau_1}} [\sigma_0^{n+1} - \sigma_0^n], \tag{14}$$

where D^e is the fourth-order tensor that is analogous to the elastic spring constant μ_0 in the one-dimensional case. Hence, the response of the two SLS in series can be computed individually using Eq. (1) so that we obtain $u_{dashpot}$ (which is the nodal displacement from the first SLS that mimics the response of the dashpot in the three-parameter fluid model) and u_{voigt} (which is the nodal displacement from the second SLS that mimics the response of the Voigt element in the three-parameter fluid model). Using Boltzmann's principle of superposition [18], the total nodal displacement vector u will then be given by the sum of $u_{dashpot}$ and u_{voigt}.

[1] S. Huang and D. E. Ingber, Nat. Cell Biol. **1**, E131 (1999).
[2] H. Huang, R. D. Kamm, and R. T. Lee, Am. J. Physiol.: Cell Physiol. **287**, C1 (2004).
[3] D. E. Ingber, Ann. Med. **35**, 564 (2003).
[4] N. Wang, J. P. Butler, and D. E. Ingber, Science **260**, 1124 (1993).
[5] N. Wang and D. E. Ingber, Biophys. J. **66**, 2181 (1994).
[6] A. Moustakas and C. Stournaras, J. Cell. Sci. **112**, 1169 (1999).
[7] O. Thoumine and A. Ott, Biorheology **34**, 309 (1997).
[8] K. A. Ward, W. I. Li, S. Zimmer, and T. Davis, Biorheology **28**, 301 (1991).
[9] R. E. Mahaffy, C. K. Shih, F. C. MacKintosh, and J. Kas, Phys. Rev. Lett. **85**, 880 (2000).
[10] M. Lekka, P. Laidler, D. Gil, J. Lekki, Z. Stachura, and A. Z. Hrynkiewicz Eur. Biophys. J. **28**, 312 (1999).
[11] J. Sleep, D. Wilson, R. Simmons, and W. Gratzer, Biophys. J. **77**, 3085 (1999).
[12] J. Guck *et al.*, Biophys. J. **88**, 3689 (2005).
[13] B. Lincoln, H. M. Erickson, S. Schinkinger, F. Wottawah, D. Mitchell, S. Ulvick, C. Bilby, and J. Guck, Cytometry, Part A **59A**, 203 (2004).
[14] F. Wottawah, S. Schinkinger, B. Lincoln, R. Ananthakrishnan, M. Romeyke, J. Guck, and J. Kas, Phys. Rev. Lett. **94**, 098103 (2005).
[15] R. Ananthakrishnan, J. Guck, F. Wottawah, S. Schinkinger, B. Lincoln, M. Romeyke, T. Moon, and J. Kas, J. Theor. Biol. **242**, 502 (2006).
[16] J. Guck, R. Ananthakrishnan, H. Mahmood, T. J. Moon, C. C. Cunningham, and J. Kas, Biophys. J. **81**, 767 (2001).
[17] F. Wottawah, S. Schinkinger, B. Lincoln, S. Ebert, K. Muller, F. Sauer, K. Travis, and J. Guck, Acta Biomater. **1**, 263 (2005).
[18] W. N. Findley, J. S. Lai, and K. Onaran, *Creep and Relaxation of Non-Linear Viscoelastic Materials, With an Introduction to Linear Viscoelasticity* (North-Holland Publishing Co., Amsterdam, 1976).
[19] F. Guilak, J. R. Tedrow, and R. Burgkart, Biochem. Biophys. Res. Commun. **269**, 781 (2000).
[20] M. Sato, N. Ohshima, and R. M. Nerem, J. Biomech. **29**, 461 (1996).
[21] O. Thoumine and A. Ott, J. Cell. Sci. **110**, 2109 (1997).

[22] A. R. Bausch, W. Moller, and E. Sackmann, Biophys. J. **76**, 573 (1999).
[23] B. D. Hoffman, G. Massiera, K. M. Van Citters, and J. C. Crocker, Proc. Natl. Acad. Sci. U.S.A. **103**, 10259 (2006).
[24] Y. Tseng, T. P. Kole, and D. Wirtz, Biophys. J. **83**, 3162 (2002).
[25] S. Yamada, D. Wirtz, and S. C. Kuo, Biophys. J. **78**, 1736 (2000).
[26] V. M. Laurent, R. Fodil, P. Canadas, S. Fereol, B. Louis, E. Planus, and D. Isabey, Ann. Biomed. Eng. **31**, 1263 (2003).
[27] M. L. Gardel, J. H. Shin, F. C. MacKintosh, L. Mahadevan, P. Matsudaira, and D. A. Weitz, Science **304**, 1301 (2004).
[28] M. L. Gardel, F. Nakamura, J. Hartwig, J. C. Crocker, T. P. Stossel, and D. A. Weitz, Phys. Rev. Lett. **96**, 088102 (2006).
[29] O. C. Zienkiewicz and R. L. Taylor, *The Finite Element Method. Basic Formulation and Linear Problems*, 4th ed. (McGraw-Hill, London, 1989), Vol. 1.
[30] F. C. MacKintosh, J. Kas, and P. A. Janmey, Phys. Rev. Lett. **75**, 4425 (1995).
[31] K. L. Sung, C. Dong, G. W. Schmid-Schonbein, S. Chien, and R. Skalak, Biophys. J. **54**, 331 (1988).
[32] G. I. Zahalak, W. B. McConnaughey, and E. L. Elson, J. Biomech. Eng. **112**, 283 (1990).
[33] L. Eichinger, B. Koppel, A. A. Noegel, M. Schleicher, M. Schliwa, K. Weijer, W. Witke, and P. A. Janmey, Biophys. J. **70**, 1054 (1996).
[34] M. Radmacher, M. Fritz, C. M. Kacher, J. P. Cleveland, and P. K. Hansma, Biophys. J. **70**, 556 (1996).
[35] G. K. Ragsdale, J. Phelps, and K. Luby-Phelps, Biophys. J. **73**, 2798 (1997).
[36] A. R. Bausch, F. Ziemann, A. A. Boulbitch, K. Jacobson, and E. Sackmann, Biophys. J. **75**, 2038 (1998).
[37] F. Guilak, G. R. Erickson, and H. P. Ting-Beall, Biophys. J. **82**, 720 (2002).
[38] P. A. Valberg and D. F. Albertini, J. Cell Biol. **101**, 130 (1985).
[39] B. Martinac, J. Cell. Sci. **117**, 2449 (2004).
[40] S. Sukharev and D. P. Corey, Sci. STKE **2004**, re4 (2004).
[41] S. Munevar, Y.-L. Wang, and M. Dembo, J. Cell. Sci. **117**, 85 (2004).
[42] P. A. Janmey, Physiol. Rev. **78**, 763 (1998).
[43] J. S. H. Lee, P. Panorchan, C. M. Hale, S. B. Khatau, T. P. Kole, Y. Tseng, and D. Wirtz, J. Cell. Sci. **119**, 1760 (2006).
[44] M. Kaliske and H. Rothert, Comput. Mech. **19**, 228 (1997).